Grasso, L., and Coauthors, 2020: Application of the GOES-16 Advanced Baseline Imager: Morphology of a preconvective environment on 17 April 2019. *Electronic J. Severe Storms Meteor.*, **15** (2), 1–24.

Electronic Journal of
SEVERE STORMS METEOROLOGY

Application of the GOES-16 Advanced Baseline Imager: Morphology of a Preconvective Environment on 17 April 2019

LEWIS GRASSO, DAN BIKOS, JACK DOSTALEK, TING-CHI WU, KYLE HILBURN, ED SZOKE, AND JOREL TORRES
Cooperative Institute for Research in the Atmosphere
Colorado State University, Fort Collins, Colorado

JON W. ZEITLER
NOAA/NWS Austin-San Antonio Weather Forecast Office
New Braunfels, TX

WILLIAM E. LINE
NOAA/NWS Pueblo Weather Forecast Office
Pueblo, CO

ARIEL E. COHEN
NOAA/NWS Miami Weather Forecast Office
Miami, FL

(Submitted 29 October 2019; in final form 17 April 2020)

ABSTRACT

Thunderstorms formed in the afternoon of 17 April 2019 over northern Mexico. Satellite data are used to highlight several features associated with convective preconditioning over portions of Coahuila, Mexico. Satellite imagery was used to identify two preconvective features over northern Coahuila: 1) A relatively moist boundary layer inferred from channel differencing of imagery near 10.3 μm and 12.3 μm, and 2) Upward vertical motion inferred from decreasing values of brightness temperatures near 7.34 μm (low-level water vapor). Due to the approach of a trough at 500 hPa, a larger region of cooling was evident in low-level water vapor imagery. Evidence of blowing dust in imagery was used to highlight a wind-shift boundary along with a possible region of enhanced horizontal convergence. A demonstration of a time-of-arrival tracking feature is used to show a benefit to a forecaster in determining the arrival of a region of blowing dust, possible enhanced horizontal convergence and subsequent convective initiation. Assimilation of satellite data that contains key features and potential benefits to numerical weather prediction is addressed. Convective preconditioning of an environment outside of the United States, but adjacent to a U.S. county warning area, is an important situation to monitor as subsequent convection may move into a forecaster's region of responsibility.

1. Introduction

Important characteristics of the vertical and horizontal distribution of water vapor are important for the preconvective storm environment. Several methods have been developed to retrieve the vertical distribution of water vapor with the use of sounder data onboard geostationary satellites. In addition, the horizontal distribution of water vapor, particularly in the planetary boundary layer, has been described through the use of not only hyperspectral techniques, but also individual infrared bands (Purdom 1976; Hillger and Vonder Haar 1977; Chesters et al. 1983; Zehr et al. 1988; McMillin et al. 1995; Rao and Fuelberg 1997; Bikos et al. 2006).

Corresponding author address: Lewis Grasso, Colorado State University, 1375 Campus Delivery, Fort Collins, CO 80523-1375, E-mail: Lewis.Grasso@colostate.edu

Forecasting the location and timing of convective initiation has been and remains a challenging problem. At issue is the ability to identify features in the preconvective environment that may lead to convective development. Banacos and Schultz (2005) compared and contrasted the use of moisture flux convergence (MFC) and horizontal mass convergence to aid in the identification of surface boundaries. Results pointed to an advantage of horizontal mass convergence over MFC.

Along with other MFC sources, satellite imagery has been used to provide boundary-layer motions to aid in the calculation of MFC (Negri and Vonder Haar, 1980). Mecikalski et al. (2008, 2015) and Mecikalski and Bedka (2006) combined radar and satellite data to monitor the temporal evolution of observed cumulus clouds for convective initiation. In the Mecikalski studies, convective initiation was defined by the existence of cumulus clouds and values of radar reflectivity >35 dB*Z*.

At times, observations of processes relevant to convective initiation may be unattainable. Numerical models then may be used as guidance by providing information at locations that are unobservable by directly sensed observations. For example, Houston and Niyogi (2007) used a cloud model to investigate the sensitivity of convective initiation from two competing processes: 1) Increase in parcel buoyancy due to upward vertical motion and 2) decrease in parcel buoyancy due to mixing with the near environment. One aspect of the study related to convective preconditioning may be the impact vertical motion has on environmental lapse rates. Vertical motion may be a result of a variety of mechanisms as listed in Tables 3.1 and 3.2 of Johnson and Mapes (2001). More recently, Madaus and Hakim (2016) examined anomalies in surface observations in relation to convective initiation. In particular, they point to the underused weather observations obtained by private citizens (Madaus et al. 2014; Mass and Madaus 2014).

Advanced four-dimensional data assimilation (FDDA) techniques were shown to improve forecasting of convection during the International H_2O Project 2002 (IHOP_2002). Specifically, Childs et al. (2006) used an experimental FDDA system that improved surface fluxes. Results showed improvements in the numerical forecasting of convective development. As part of IHOP_2002, Xue and Martin (2006) numerically simulated a Texas Panhandle dryline, to show the importance of the interaction of horizontal convective rolls (Atkins et al. 1998) with the dryline and subsequent convective initiation.

This paper concentrates on convective preconditioning over northern portions of the state of Coahuila, Mexico, which occurred on 17 April 2019. Specifically, preconditioning occurred over the Serranias Del Burro mountain range in northern Coahuila, which extends northwestward from El Judio, to El Bonito, and finally to the Mexico-United States border (Fig. 1). Thunderstorm development over northern Coahuila is important to forecasters in Texas, since newly formed convection can cross into Texas and impact the county warning areas (CWAs) of the Midland, Austin-San Antonio, and Corpus Christi National Weather Service (NWS) forecast offices. Further, the impact of convection crossing international borders extends to any public and private forecasting agency, along with local emergency managers.

Organization of this paper is as follows: A brief overview of data from two types of satellite platforms are provided in section 2. A detailed description of the 17 April 2019 case study is found in section 3. Additionally, section 3 contains several subsections. The discussion of the preconvective environment is divided into two time periods in which the morphology of events is detailed, along with an interpretation of physical processes related to convective preconditioning. Forecaster perspective of the case herein, along with potential data assimilation applications, are found in section 4, while the last section contains the summary and conclusions.

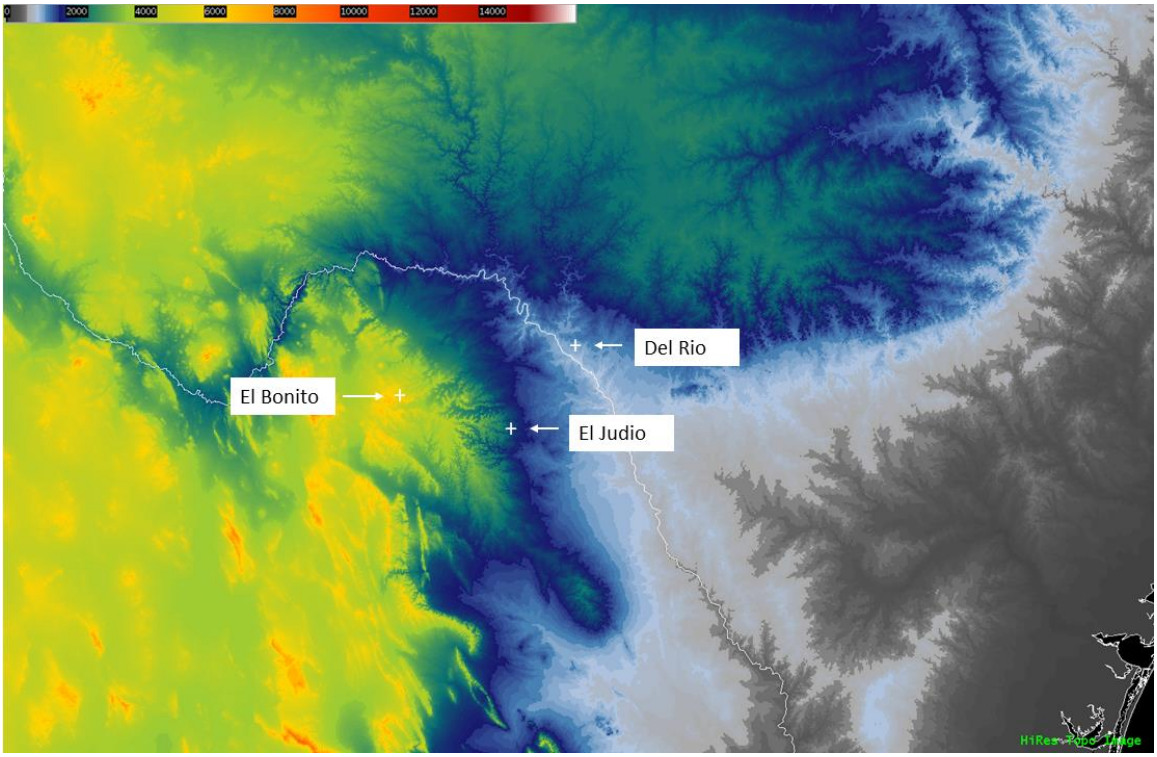

Figure 1: Advanced Weather Interactive Processing System (AWIPS) topographical height (ft MSL) indicating the Serranias Del Burro in Coahuila, Mexico. Resolution of this data is 1.0 km. *Click image to enlarge.*

2. Data

As part of the beginning of the GOES-R program, which encompasses the GOES-R, -S, -T, and -U satellites, GOES-R was launched in 2016 and soon became operational and identified as GOES-16, positioned near 75W and the Equator (Schmit et al. 2017, 2018). Onboard GOES-16, the Advanced Baseline Imager (ABI) collects information at sixteen spectral bands, along with the following spectrally dependent instantaneous geometric fields of view: 0.5, 1.0, and 2.0 km (Kalluri et al. 2018). In preparation for ABI data, many convective applications of data from ABI have been developed. For example, Lindsey et al. (2014, 2018) discuss identification of the deepening of low-level moisture and subsequent cloud development. A convective initiation algorithm has been developed by Walker et al. (2012), while Cintineo et al. (2014, 2018) discuss an algorithm that assigns a severity potential to existing convection. Bedka et al. (2018) describe the relationship between above-anvil cirrus and severe weather. Super rapid scan capabilities of ABI have been studied by Apke et al. (2018), in which they detail the relationship between thunderstorm-top-derived flows and convective updrafts. Further, operational applications of super rapid scan imagery by forecasters at the Storm Prediction Center are outlined in Line et al. (2016).

Satellite images in this manuscript are mainly from ABI onboard GOES-16 on 17 April 2019. However, a few images from the Visible Infrared Imaging Radiometer Suite (VIIRS) onboard two Low Earth Orbiting (LEO) platforms, S-NPP and NOAA-20, are also discussed. In order to display results, this study utilized the Advanced Weather Interactive Processing System (AWIPS). AWIPS was used for GOES-R satellite product demonstration, which included a variety of weather applications (Goodman et al. 2012). A distinct advantage of AWIPS is the ability to overlay plots of model data, surface observations, and satellite data, such as GOES-16 and NOAA-20 brightness temperatures (T_b) and values of reflectance.

Application of the split window difference (SWD)—defined as ABI values of T_b (10.3 μm) – T_b (12.3 μm)—has been discussed by Lindsey

et al. (2014, 2018). Values of T_b near 10.3 μm are combined with values of the SWD and will be referred to as the SWD/IR Overlay, similar to that of Setvák et al. (2013). The SWD/IR Overlay product is an AWIPS procedure that is available for download on the NOAA Virtual Lab[1]. Values of T_bs near 10.3 μm and <–10°C are rainbow-color enhanced to capture cloud tops for convective events, while values of the SWD from –2°C to 10°C, are displayed as gray shades.

SWD imagery from the GOES-R series provides forecasters with a low-latency tool to fill a spatial and temporal gap that exists in observed horizontal moisture information. Specifically, the SWD is used by NWS forecasters to identify not only low-level moisture gradients—for example, a dryline, but also localized low-level moisture prior to the growth of cumulus clouds and associated initiation of deep moist convection.

Optimal conditions for use of the SWD are clear-sky scenes (no clouds). Cirrus cloud layers may be undetectable in visible imagery during the daytime, and skies may appear clear; yet, evidence of the cirrus layers will be not only conspicuous in the SWD, but also prevent the morphology of low-level water vapor from being observed.

Historically, forecasters would use networks of surface observations or objective analysis systems to locate and track low-level moisture features. These observing networks typically have a spatial resolution on the order of dozens of km and temporal resolution up to hourly. From GOES-R series satellites, nadir footprint sizes of 2 km and temporal sampling of 5-min for CONUS, along with 30-s to 1-min sampling for mesoscale sectors, affords a means of detecting and tracking moisture features with improved detail and reduced latency. The improved detail increases confidence regarding the location of significant moisture features and related potential future convective initiation.

At times, NWS forecasters may be overwhelmed by the volume of available data. As a result, priority is given to effective and efficient displays of information. The SWD/IR Overlay was created in order to combine the strengths of both products for use in convective situations. As described, the benefit of the SWD in convective circumstances is realized only for clear-sky pixels. Therefore, the inclusion of T_bs near 10.3 μm for clouds tops as an overlay adds value to the overall display, while the integrity of the SWD is maintained. A forecaster can monitor moisture features in clear-sky areas, while at the same time diagnose convective development and cloud-top trends in the cloudy areas. The grayscale color table for the SWD, combined with the rainbow color table for the 10.3 μm channel, includes enough contrast to differentiate the two products easily. The addition of surface observations as an overlay supplements the SWD representation of the location and evolution of low-level moisture. On clear days when the SWD/IR Overlay is in use, visible imagery may be loaded in a separate panel, in order to diagnose the evolution of a cumulus cloud field and eventual convective initiation.

3. Case study of 17 April 2019

On the morning of 17 April 2019, an upper-level low existed over the southern Rockies (Fig. 2). East of the upper-level low, strong flow (40–50 kt at 500 hPa) was observed in northern Mexico and western Texas. In response, a surface low-pressure area existed from western Kansas southwestward through Texas and into northern Mexico (Fig. 3). A cold front extended southwestward from the primary surface low in western Kansas and merged with a dryline in New Mexico that extended southward into northern Mexico. The warm sector east of the dryline, with origins from the Gulf of Mexico, was characterized by surface dewpoints between 17–21°C (60s to low 70s °F). In sharp contrast, drier air to the west of the dryline, with origins from the desert plateaus of western North America, had surface dewpoints from –1°C to 3°C (30s °F).

a. Morphology of preconvective environment: 1816–2026 UTC

Spatial, temporal, and spectral capabilities of ABI represent a significant advancement over previous GOES imagers and sounders (Schmit et al. 2018; Schmit et al. 2017; Kalluri et al. 2018). Before presenting an animation of ABI data from 1816 UTC to 2026 UTC 17 April 2019, a preliminary discussion is given that will concentrate on imagery at 1926 UTC 17 April

[1] https://vlab.ncep.noaa.gov/web/stor/goes

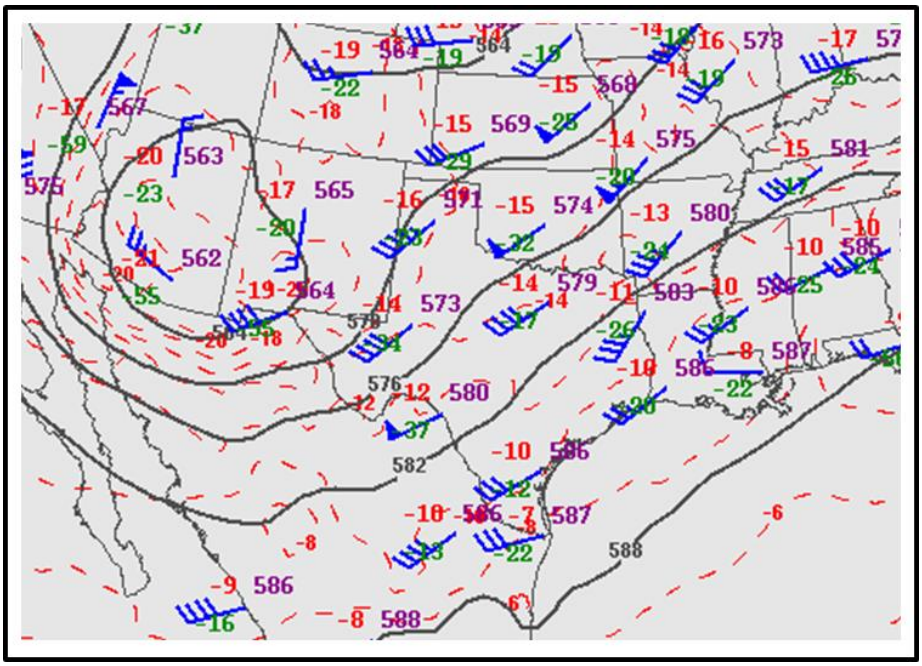

Figure 2: 500-hPa map at 1200 UTC 17 April 2019 showing geopotential heights (dm), isotherms and dewpoint depression (°C), and wind barbs (kt) where solid triangles represent 50 kt (26 m s^{-1}), long and half wind barbs represent 10 kt (5 m s^{-1}) and 5 kt (2.6 m s^{-1}), respectively. Image from Storm Prediction Center.

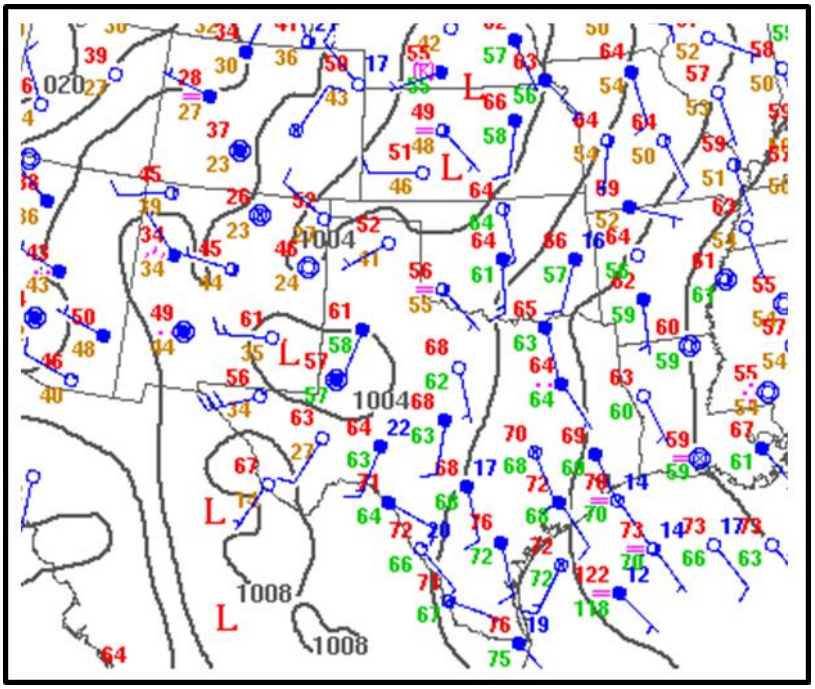

Figure 3: Surface map at 1200 UTC 17 April 2019 showing temperature and dewpoint (°F), contours of pressure (hPa), and wind barbs (kt). Image from Storm Prediction Center.

2019 to aid the reader in the identification of features—blowing dust and cooling in the low-level water vapor imagery, for example—that had yet to develop at early times of the 130-min loop.

A demarcation existed between dry (darker gray) and moist (lighter gray) boundary-layer air, which extended from Mexico, through Coahuila (black oval in Fig. 4), to Texas. Values of GOES-16 reflectance near 0.64 μm is shown in Fig. 5—typically referred to as the "red visible" will hereafter be referred to as visible—was unable to reveal water-vapor boundaries exhibited in Fig. 4. In particular, skies were clear in the region of interest in northern Coahuila. A few important features located in the lower troposphere were undetectable in both Figs. 4 and 5.

Two features in ABI imagery near 7.34 μm (Fig. 6)—hereafter referred to as the low-level water vapor—were relevant to convective preconditioning. The first was that the largest values of T_bs existed over elevated plateaus of Mexico (compare Figs. 1 and 6). Diurnal mixing on the elevated terrain of northern Mexico frequently results in a dry-adiabatic boundary layer during the spring. In response to southwesterly winds associated with the approach of an upper level trough (Fig. 2), the hot, well-mixed layer was advected northeastward to setup an elevated mixed layer (EML; Carlson and Ludlam 1968; Lanicci and Warner 1991a) over the region of interest in northern Mexico into Texas. EMLs enhance the potential for severe convection by maintaining 1) a low-level capping inversion along with 2) a nearly dry adiabatic lapse rate above the level of free convection (LFC). If convection initiates in such an environment, the probability for all types of severe weather increase (Carlson et al. 1983; Farrell and Carlson 1989; Lanicci and Warner 1991b; Ribeiro and Bosart 2018).

Important forecasting implications exist when EMLs are present. In particular, when the LFC exists near the base of an EML, rising parcels will experience enhanced upward acceleration during ascent through an EML, potentially leading to the development of "explosive" growth of thunderstorms.

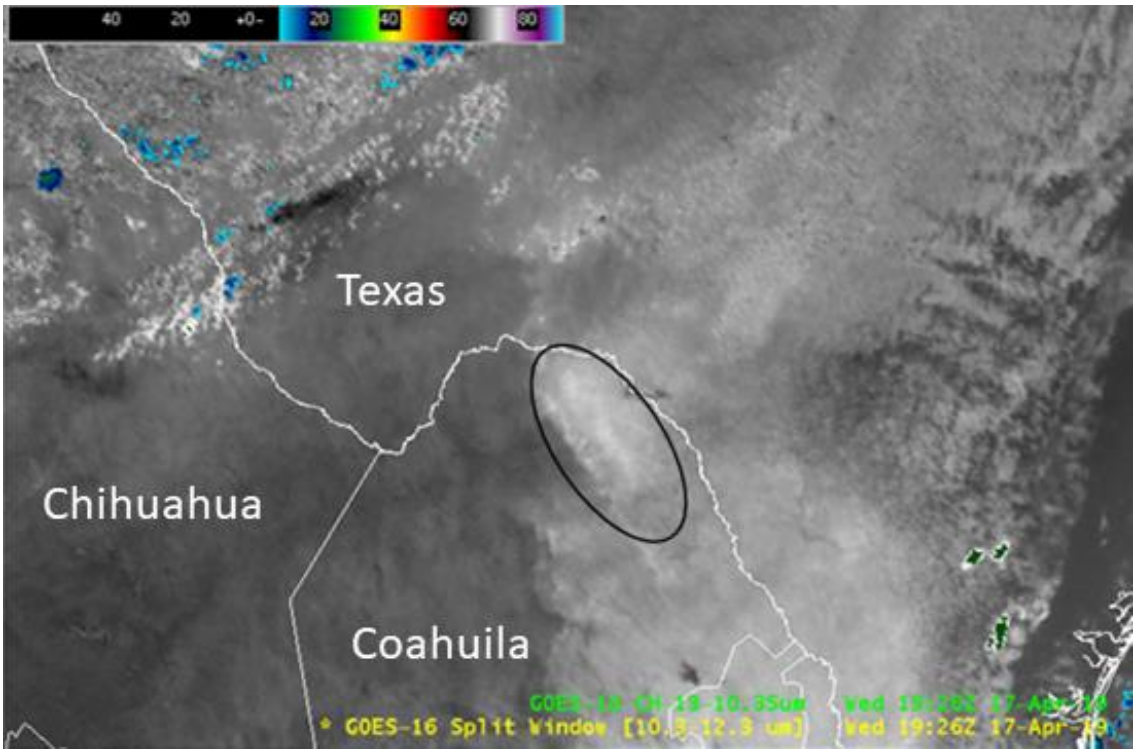

Figure 4: GOES-16 ABI imagery at 1926 UTC 17 April 2019 showing the SWD/IR Overlay.

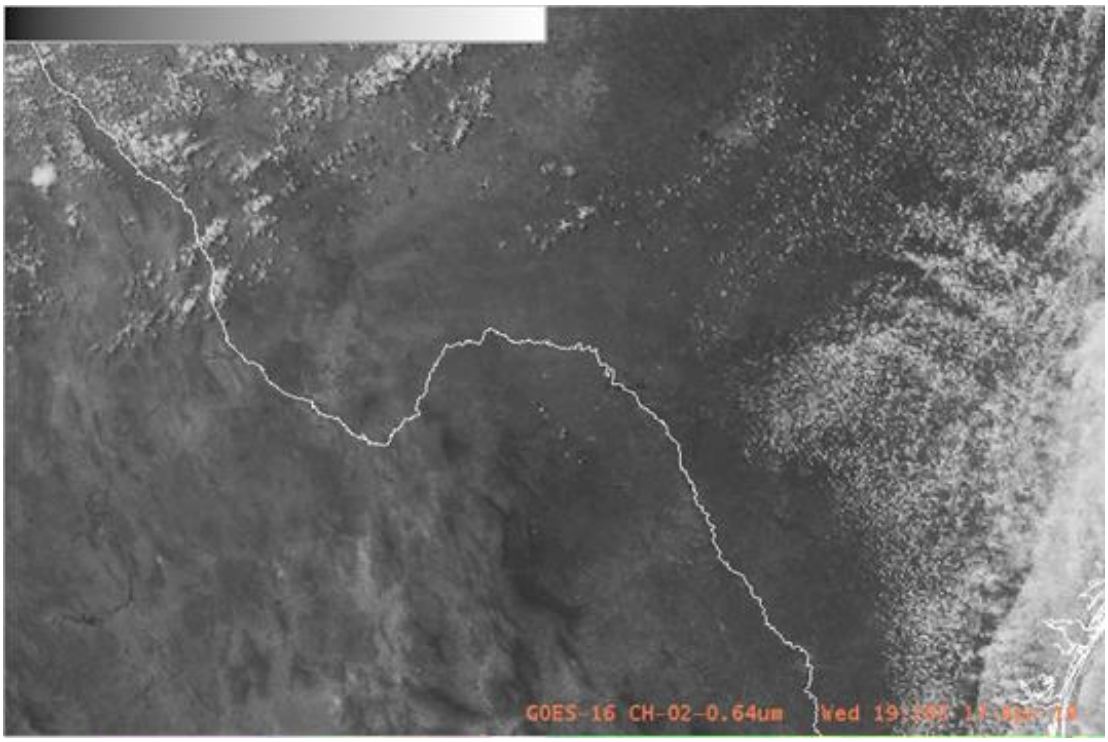

Figure 5: GOES-16 ABI imagery at 1926 UTC 17 April 2019 showing visible imagery (reflectance near 0.64 μm).

In Fig. 6, the source of the EML was revealed by the warmest T_bs (yellow) over elevated terrain of Mexico, located in the lower left corner of the figure. As a result of southwesterly flow, the EML with T_bs of ≈5 °C, moved northeastward, over the region of interest (oval in Fig. 4) and into Texas. Both a capping inversion and nearly dry adiabatic lapse rates in the lower to mid troposphere were evident in the 1200 UTC 17 April 2019 sounding at Del Rio, TX (DRT; Fig. 7). Clear skies allowed for EML tracking with this event, as the EML advected over the region of interest.

Values of T_bs in the low-level water vapor imagery also can be understood through the use of the vertical distribution of a weighting function (Liou 1980; Weldon and Holmes 1991). In general, a weighting-function plot indicates the region in the Earth-atmosphere system where radiant energy originates that subsequently is detected by a satellite at a specific wavelength range. A vertical plot of the weighting function for the low-level water vapor band near 7.34 μm, which was computed from the 1200 UTC 17 April 2019 DRT sounding, is displayed in Fig. 8. As seen in the figure, radiant energy detected by ABI originated in the region bounded by the vertical axis and the curve of the weighting function. Further, nearly dry adiabatic lapse rates existed in the DRT sounding from ≈850–500 hPa (Fig. 7)—a characteristic of an EML. A comparison between Figs. 7 and 8 indicates that the nearly dry adiabatic layer from 850–500 hPa in Fig. 7 was bounded by the weighting-function curve in Fig. 8, and aids in understanding why T_bs near 7.34 μm are important in the identification of EMLs, when cloud obscuration is absent. Gitro et al. (2019) demonstrated the utility of ABI data near 7.34 μm and sounding analysis in tracking an EML.

A second feature in ABI imagery of the low-level water vapor (Fig. 6) to note is the rather unimposing and approximately linear segment of cooler T_bs (indicated by white arrows) over Coahuila. Importantly, the linear segment of cooler T_bs was collocated with the dry (dark gray) and moist (light gray) boundary evident in Fig. 4. Boundaries in the SWD can be due to regions of horizontal convergence at the surface or blocking of moist air by topographical ridges. In this case, the boundary in the SWD was adjacent to elevated topography in Coahuila (Fig. 1).

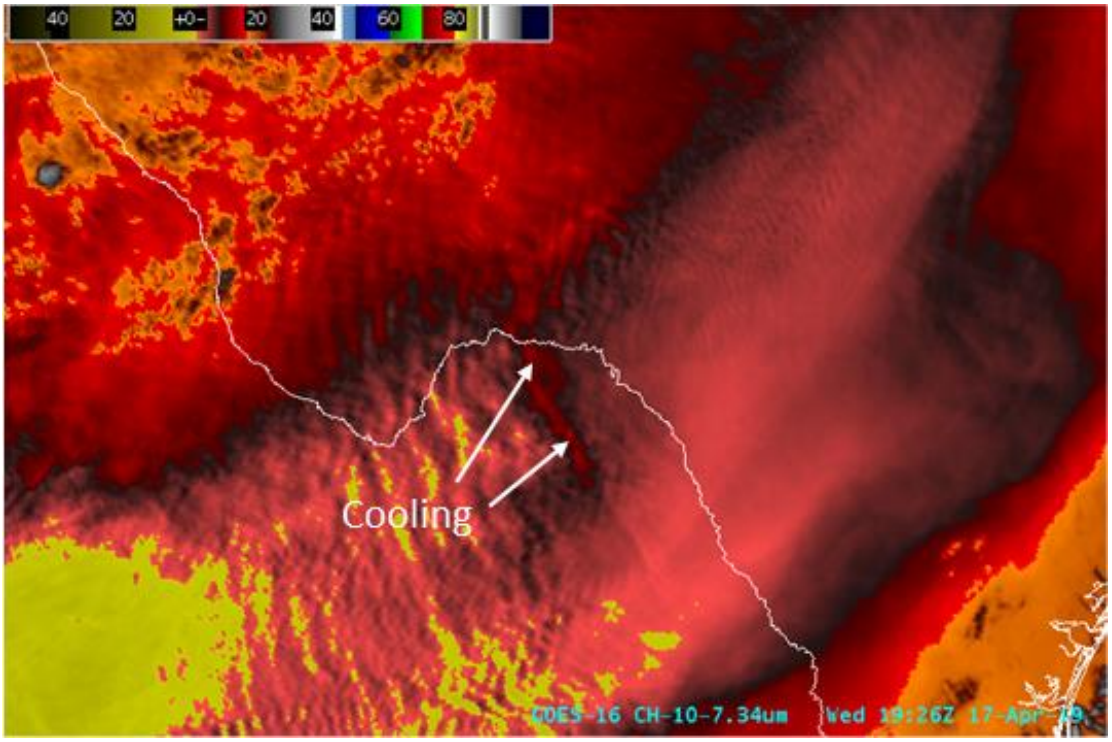

Figure 6: GOES-16 ABI imagery at 1926 UTC 17 April 2019 showing T_bs near 7.34 μm (low-level water vapor).

The ability to diagnose a given feature in a satellite image may vary as a function of the color table used. Occasionally regions of interest may exhibit a sharp contrast with nearby features and become easily identified. However, other features may be challenging to identify with a fixed color enhancement due to subtle or insufficient contrast with the background. As a result, the use of different color enhancements to notice multiple features is encouraged. An example of an atmospheric feature potentially requiring color-table adjustments is blowing dust.

Blowing dust can produce values of the SWD as small as –5°C. Since the SWD example in Fig. 4 uses a linear color table and a data range from –2°C to +10°C, the blowing dust signal was somewhat subdued. With a change of color enhancement and expanded data range from –15°C to +15°C, two regions of blowing-dust became more evident (Fig. 9). Consequently, blowing dust in Fig. 9 appears purple and exhibits improved contrast with the background. As blowing dust is in response to mechanical erosion of the surface by near-surface winds, the movement of blowing dust in regions where surface observations are lacking—both spatially and temporally—provides valuable information to a forecaster.

The western edge of the moist layer also is evident near the center of Fig. 9 over northern Coahuila. As stated in the beginning of section 2, the size of the sub-satellite footprint for ABI data used to produce the SWD is 2.0 km. In contrast, the size of the sub-satellite footprint for VIIRS data that can be used to produce SWD imagery is 750 m.

S-NPP and NOAA-20 fly in a common polar-orbital plane, about ½ orbit apart. Both satellites passed over the region of interest during the afternoon on 17 April 2019. Consequently, SWD imagery, T_b (10.76 μm) – T_b (12.01 μm), was made from VIIRS onboard S-NPP valid at 1939 UTC (Fig. 10a) and VIIRS onboard NOAA-20 valid at 2030 UTC (Fig. 10b).

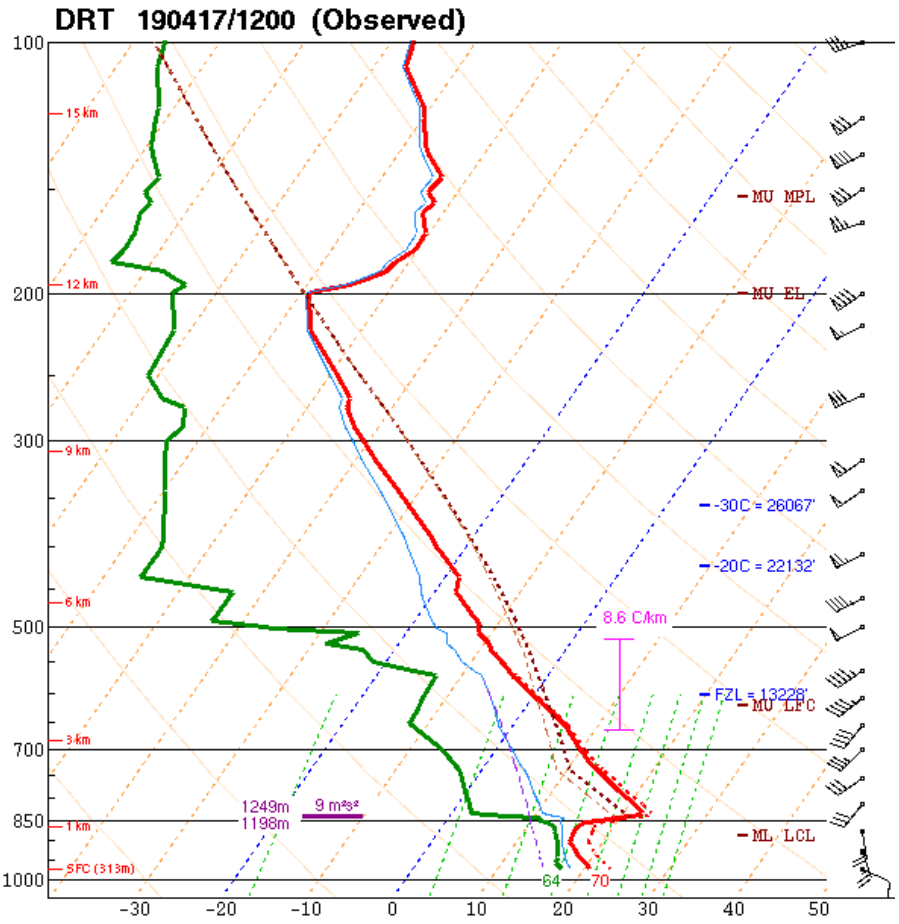

Figure 7: Skew *T*–log*p* presentation of the observed sounding at Del Rio, TX, 1200 UTC 17 April 2019. Image from Storm Prediction Center.

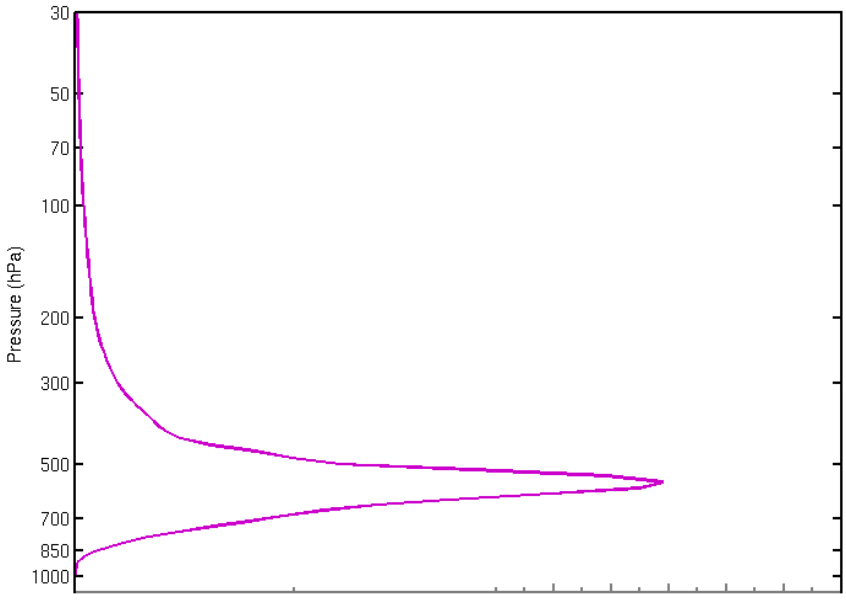

Figure 8: Weighting function for 7.34 μm from the Del Rio, TX sounding (Fig. 7). Real-time weighting function profiles are available at the following CIMSS website: https://cimss.ssec.wisc.edu/goes/wf/.

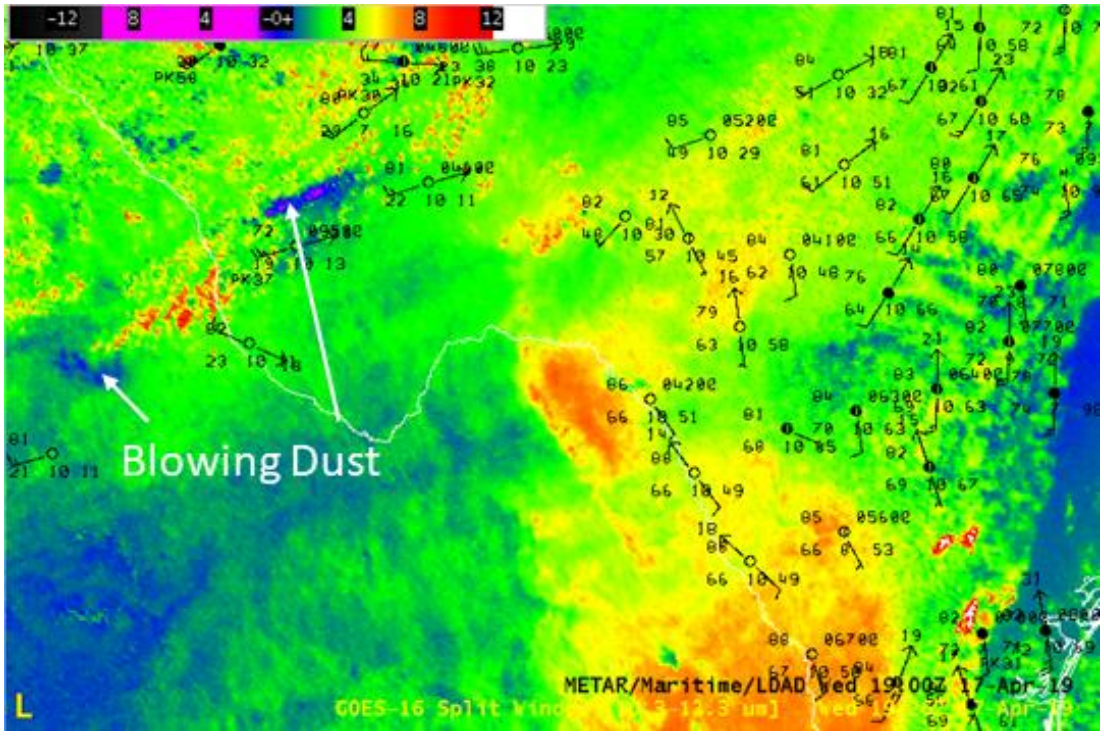

Figure 9: GOES-16 ABI SWD and surface observations at 1926 UTC 17 April 2019.

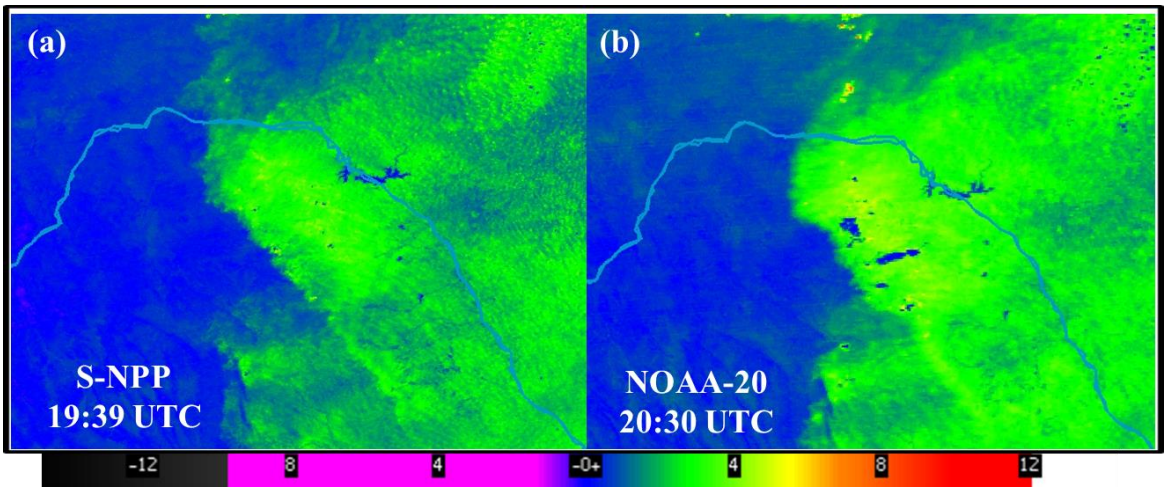

Figure 10: VIIRS SWD, T_b (10.76 μm) – T_b (12.01 μm), onboard a) S-NPP at 1939 UTC and b) NOAA-20 at 2030 UTC on 17 April 2019. Note: the color table and range are identical to that in Fig. 9. *Click image to enlarge.*

A direct comparison of the GOES-16 SWD in Fig. 9 with the VIIRS SWD in Fig. 10 highlights three features: 1) Both plots, Figs. 9 and 10, use the same color enhancement table, 2) Figs. 9 and 10a are separated by a few minutes, and 3) The plots in Fig. 9 and Fig. 10 appear different. Despite the same color enhancement table, Figs. 9 and 10 appear different due to the different central wavelengths and spectral band widths of the respective imagers. Note the differences in values of the central wavelengths in T_b (10.35 μm) – T_b (12.3 μm) for ABI and T_b (10.76 μm) – T_b (12.01 μm) for VIIRS. Further, the ABI spectral width for T_bs near 10.35 μm ranges from 10.1 μm to 10.6 μm; the VIIRS spectral width for T_bs near 10.76 μm ranges from

10.26 μm to 11.26 μm. Quantitatively, both VIIRS channel differences exhibit the moist boundary layer within the region of interest, as indicated by the oval in Fig. 4.

As usual, animated satellite imagery provides additional information compared to a single image. That said, Figs. 4, 5, 6, and 9 are displayed together in an animation (Fig. 11) beginning at 1816 UTC and ending 2026 UTC 17 April 2019. From 1816–2026 UTC, the western edge of a moist boundary layer was evident as a quasistationary boundary from dark to light gray in Coahuila (SWD/IR Overlay in Fig. 11). As indicated by the color table, values of T_bs near 10.3 μm that were <–10°C are denoted by rainbow colors. A direct comparison of the SWD/IR Overlay (top left panel in Fig. 11) with the visible (top right panel in Fig. 11) indicate clear skies during the beginning of the time period, with the development of a few transient cumulus clouds later in the loop. In particular, visible imagery is unable to indicate the existence of a moist layer as seen in the SWD.

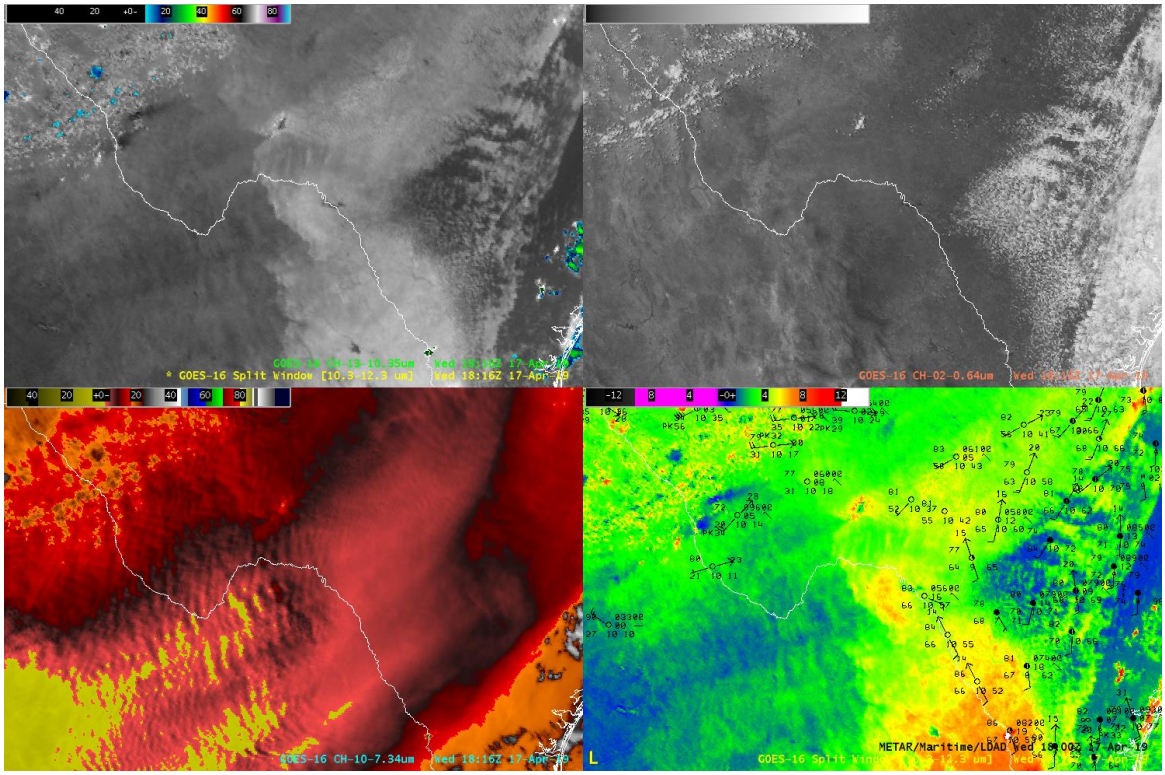

Figure 11: GOES-16 ABI animation from 1816 to 2026 UTC on 17 April 2019. Static (initial) image is at 1816 UTC 17 April 2019. Top left is the SWD/IR Overlay, top right shows visible imagery, low-level water vapor imagery is displayed in the bottom left, while the SWD is in the bottom right. *Click on the image to open animation and enlarge.*

Another temporally changing feature that is evident in the animation was the region of decreasing values of T_bs in the low-level water vapor over northern Coahuila (lower left panel in Fig. 11). A comparison of the SWD and low-level water vapor imagery shows that the upstream edge of the region of cooling was collocated with the western edge of the moist layer. In time, the region of cooling T_bs expanded downstream in response to the southwesterly flow. However, the upstream edge of the region of cooling remained quasistationary over the nearly 2-h period of the animation. In order to further illustrate the time

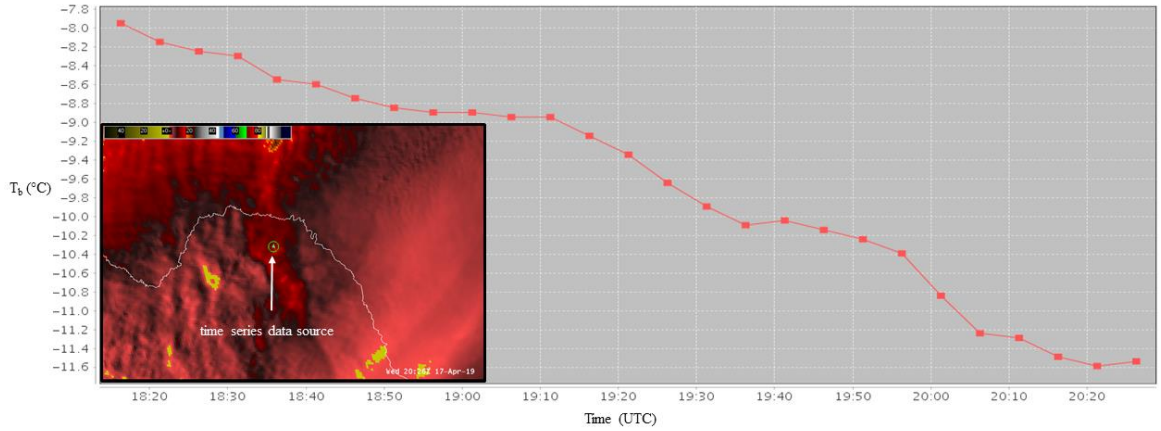

Figure 12: Time series of median values of GOES-16 ABI T_bs from low-level water vapor imagery from 1816–2026 UTC 17 April 2019. Median values were computed from ABI pixels contained in the circle denoted by a white arrow on the low-level water vapor image that is inset on the time series. *Click image to enlarge.*

tendency of values of T_bs of the low-level water vapor, a time series of median, as opposed to mean, values of T_bs is displayed in Fig. 12. Median values were used to avoid substantial variations due to passing clouds. Further, the data source of the time series was ABI pixels that were bounded by a circle—exhibited on the low-level water vapor image, which is inset on Fig. 12. As seen in the time series, values of T_bs decreased about 3.5°C during the ≈2-h time period.

Values of the SWD are displayed in the lower right panel of the animation in Fig. 11. A prominent quasistationary edge of the moist layer was evident over northern Coahuila. Surface observations indicate that temperatures were ≈30°C (upper 80s °F) with dewpoints near 18°C (mid 60s °F). Winds were from the southeast with speeds ≈5 m s^{-1} (10 kt). Farther to the west, two regions of blowing dust (purple) were evident. Surface observations indicated a southwesterly wind with speeds ≈10 m s^{-1} (20 kt) and gusts between 15–20 m s^{-1} (30–40 kt) in Texas. A second region of blowing dust was evident to the southwest of Texas in northern Chihuahua, and indicated west-northwesterly winds. In both locations, values of dewpoint temperatures were about –5°C (lower 20s °F), representing an ≈22°C (40°F) decrease in dewpoint temperatures, compared to values over northern Coahuila.

A discussion between the capabilities of ABI and past imagers on GOES platforms is warranted. First, the GOES-13 imager collected data near the following wavelengths: 0.65, 3.9, 6.48, 10.7, and 13.3 μm. Consequently, the use of the SWD to highlight the western edge of a moist boundary layer would have been impossible with the lack of data near 12.0 μm. Further, the imager also lacked the capability to collect low-level water-vapor data. However, the sounder onboard GOES-13 did collect data from which the SWD could have been produced. In addition, the sounder also collected data near 7.43 μm. Nadir footprint sizes of the sounder were about 10 km, which would have produced a somewhat smeared or blurred image, making the identification of boundaries and the region of cooling a challenge. Further, images from the sounder were hourly, which represents a significant disadvantage for monitoring rapidly changing convective environments.

b. Physical interpretation: 1816–2026 UTC

Animation of GOES-16 ABI data has provided information that can be used to suggest a possible physical interpretation of events between 1816–2026 UTC. Over the ≈2-h interval, the western boundary of the moist layer remained quasistationary over northern Coahuila. Cooling of T_bs in low-level water vapor imagery was evidence of the beginning of upward vertical motion with convergence along the western boundary of the moist layer. Ascent of air locally deepened the layer of water vapor above the western boundary of the moist layer. As a result of the increased depth of water vapor,

along with the cooling effects of ascent, T_bs in the low-level water vapor decreased. Towards the end of the animation, a few clouds developed over the western edge of the moist layer, as seen in visible imagery.

Cloud formation suggested that upward motion lifted parcels to their respective lifting condensation level (LCL). That thunderstorms had yet to develop suggested that the ascent of air, though perhaps increasing, was unable to bring parcels to their LFC. In addition, turbulent processes act to mix relatively moist ascending air, with relatively dry air within the EML. In other words, parcel theory may, at times, overestimate parcel buoyancy (Houston and Niyogi, 2007).

c. Morphology of preconvective environment: 2026 UTC 17 April 2019 to 0101 UTC 18 April 2019

Additional features of the preconvective environment became evident in satellite imagery from 2026 UTC 17 April 2019 to 0101 UTC 18 April 2019. First, values of T_bs in low-level water vapor imagery decreased from 2026–2301 UTC over a broad region of northern Coahuila (Fig 13, bottom left panel). From ≈2051–2206 UTC, deeper convective clouds were evident—not only in the SWD/IR Overlay (Fig. 13, top left) with values of T_b near 10.3 μm ≈ –30°C, but also in visible imagery (Fig. 13, top right), which subsequently were sheared and advected northeastward by the environmental flow.

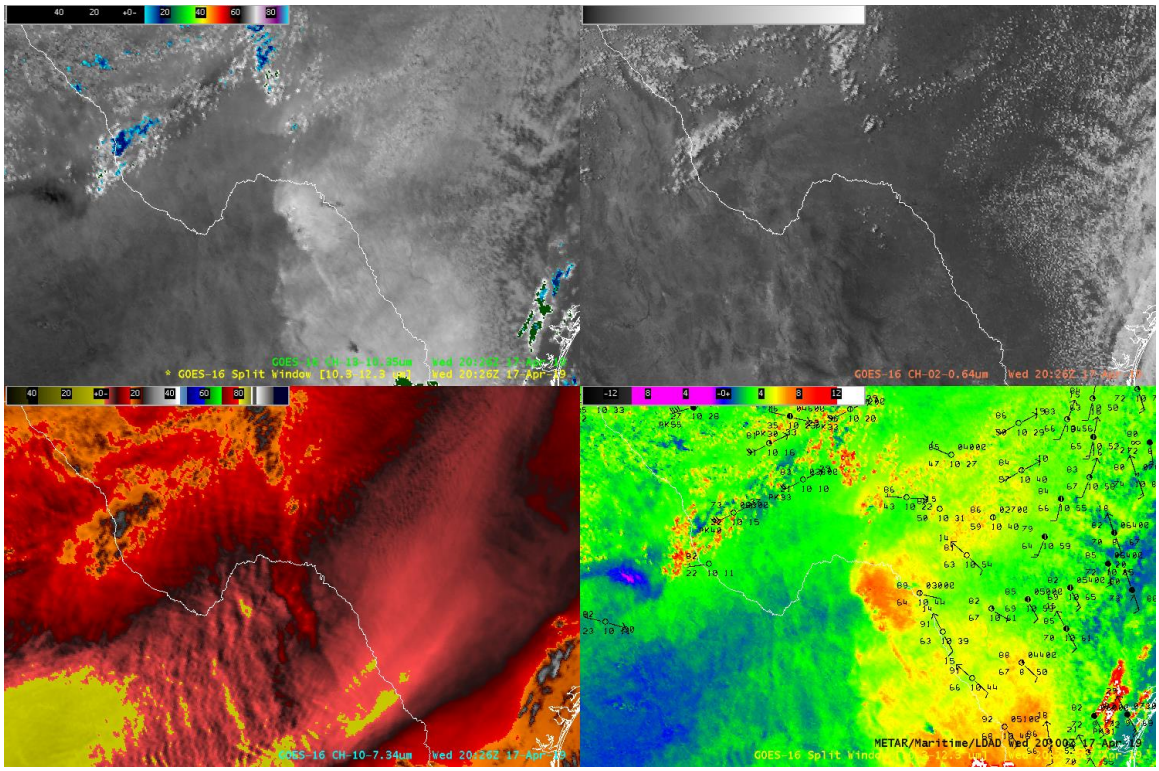

Figure 13: As in Fig. 11 but with animation from 2026 UTC 17 April 2019 to 0101 UTC 18 April 2019. *Click on the image to open animation and enlarge.*

Sheared and unsuccessful convective initiation leads to a common type of cloud material referred to as orphan anvils (Bluestein et al. 1990; Line et al. 2016; Gravelle et al. 2016). That is, during initial ascent parcels begin to breach the mixed-layer LCL. However, a capping inversion at the base of an EML suppresses vertical motion, which may prevent updrafts from reaching the LFC. During this process, vertical motion and evaporation around cumulus congestus result in cooling and moistening at the base of the EML, weakening the capping inversion and lessening the effect of dry-air entrainment for forthcoming cumulus clouds. This makes future attempts at convective initiation more likely, particularly if amplified with repeated updraft attempts phasing in the same general location as steep low-level lapse rates. GOES-16 illuminates the details of

this process much more clearly than the generation of GOES prior to the GOES-R series.

At ≈2120 UTC, a new region of blowing dust (purple) moved northeastward from western portions of Coahuila. Further, blowing dust (Fig. 13, lower right) continued to move southeastward within Chihuahua while surface winds veered from 2026–2146 UTC. At ≈2200 UTC the western edge of the moist layer—displayed in both the SWD/IR Overlay (Fig. 13 top left) and the SWD (Fig. 13 bottom right) over northern Coahuila—began moving westward. From 2026–2231 UTC, surface winds backed in the warm sector, consistent with the westward movement of the moist boundary layer. Both the change in surface winds and westward movement of the moist layer were in response to the eastward progression of the upper level low (compare Figs. 2 and 14). Thunderstorms developed at ≈2336 UTC, where the western edge of the moist layer was positioned along the Coahuila-Texas border. A second region of thunderstorms developed further south by 0011 UTC 18 April 2019, over northern Coahuila.

d. Physical interpretation: 2026–0101 UTC 18 April 2019

Two regions of blowing dust were evident in the animation displayed in Fig. 13. Northwesterly flow may be inferred from the region of blowing dust over Chihuahua, while to the southeast, southwesterly flow may be inferred from the new region of blowing dust over western Coahuila. Differential movement of both regions of blowing dust suggested a wind-shift boundary between both geographical locations. Due to the approach of an upper level trough (Fig. 14), the location of the wind-shift boundary was consistent with a cold front. Further, the broad region of decreasing values of T_bs in the low-level water vapor that occurred over northern portions of Coahuila was also consistent with the approach of an upper level trough seen in Fig. 14. Also, the western movement of the moist layer—over northern Coahuila—and northeastward movement of dust—over western Coahuila—suggested the possibility of enhanced convergence, and hence lift, along the western edge of the moist layer. Although the new region of dust was moving northeastward towards the western boundary of the moist layer, we caution that the leading edge of the blowing dust may not necessarily be the leading edge of southwesterly flow. Enhanced convergence along the western edge of the moist layer may have developed prior to the arrival of the blowing dust. As suggested by the imagery displayed in the top right panel of Fig. 13, towering cumulus formed along the western edge of the moist layer while the new region of blowing dust formed. Enhanced convergence along the western edge of the moist layer may initiate thunderstorms.

Due to the importance of the potential of enhanced convergence along the western edge of the moist layer over northern Coahuila, the utility of the time-of-arrival tool in AWIPS is discussed presently. Two different times are required by the tool here: 2156 and 2306 UTC 17 April 2019. In order for the tool to compute a linear path for extrapolation, the current time of a feature is given (2306 UTC for this case); then an earlier time is needed (2156 UTC), for the computation of the speed of a feature of interest, such as dust. Further, the location of arrival of the blowing dust is indicated by a solid black circle on the western edge of the moist layer over northern Coahuila. The black circle is indicated on all frames of the animation, and shows the extrapolated linear track of the blowing dust using imagery of the SWD (Fig. 15). Implicit in the use of the tracker in AWIPS is that a feature of interest is assumed to move with constant direction and speed.

At 2056 UTC, blowing dust became evident along the Chihuahua-Coahuila border. At 2316 UTC 17 April 2019, the tracking symbol had moved consistently with the blowing dust from 2056 UTC. However, at 2316 UTC the blowing-dust signal was no longer evident and was replaced by a quasilinear segment of clouds, which formed at ≈2311 UTC. One interpretation is that the newly formed cloud line was caused by enhanced horizontal convergence of the wind-shift boundary interacting with the southwesterly flow. By 2331 UTC, convective initiation first occurred near the Coahuila-Texas border. The orientation of the quasilinear cloud segment revealed that an extrapolation of the orientation of the cloud line to the north, in turn, showed that convective initiation occurred as the extrapolated segment intersected the western edge of the moist layer. Just to the south, at 2356 UTC, and along the western edge of the moist layer was evidence of convective initiation. However, convective initiation appeared to pulse until ≈0046 UTC 18 April 2019, when the tracked feature of interest arrived. As indicated in Fig. 15, the tracking feature in AWIPS suggested the tracking had an error of 17 min and 11 mi (18 km).

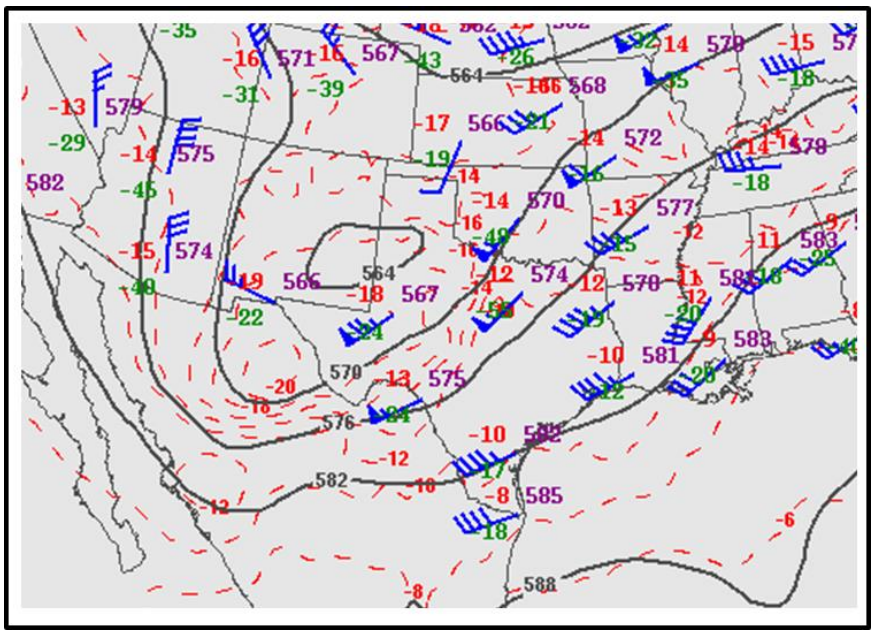

Figure 14: Same as Fig. 2 except for 0000 UTC 18 April 2019.

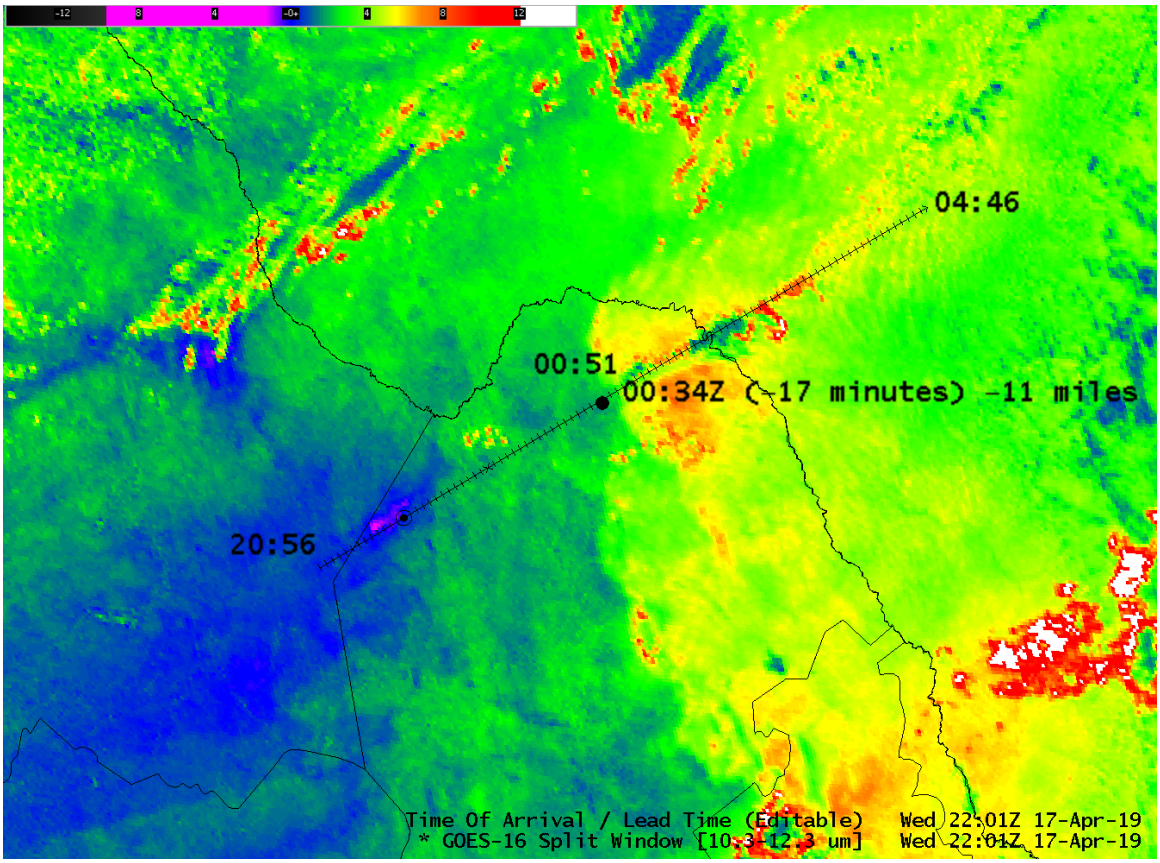

Figure 15: Time-of-arrival animation with the GOES-16 ABI SWD, from 2056 UTC 17 April 2019 to 0051 UTC 18 April 2019. *Click on the image to open animation and enlarge.*

e. WSR-88D radar signatures from 2248–0242 UTC 18 April 2019

Although the focus of this manuscript is convective preconditioning of an environment, radar signatures of the subsequent convection are shown for completeness (Fig. 16). Further, thunderstorms which formed in northern Coahuila possibly could move into the CWA of San Antonio, TX. At 2348 UTC 17 April 2019, convective development became evident by the appearance of a radar echo in northern Coahuila and the Texas border. A second echo developed slightly to the east of the first at 0030 UTC 18 April 2019. A third echo formed southwest of the second, at ≈0042 UTC 18 April 2019. As seen in the radar animation, the third echo developed into a potentially severe, right-moving supercell, which is circled in the still image of Fig. 16. Characteristics of the circled echo at 0200 UTC 18 April 2019 are the following: 1) a bounded weak-echo region; 2) largest horizontal gradient of reflectivity was on the forward right side, and 3) rightward movement. A lack of surface observations where the three storms formed over northern Coahuila attests to the value of satellite and radar data to forecasters in CWAs that may be impacted by newly developed and potentially severe convection.

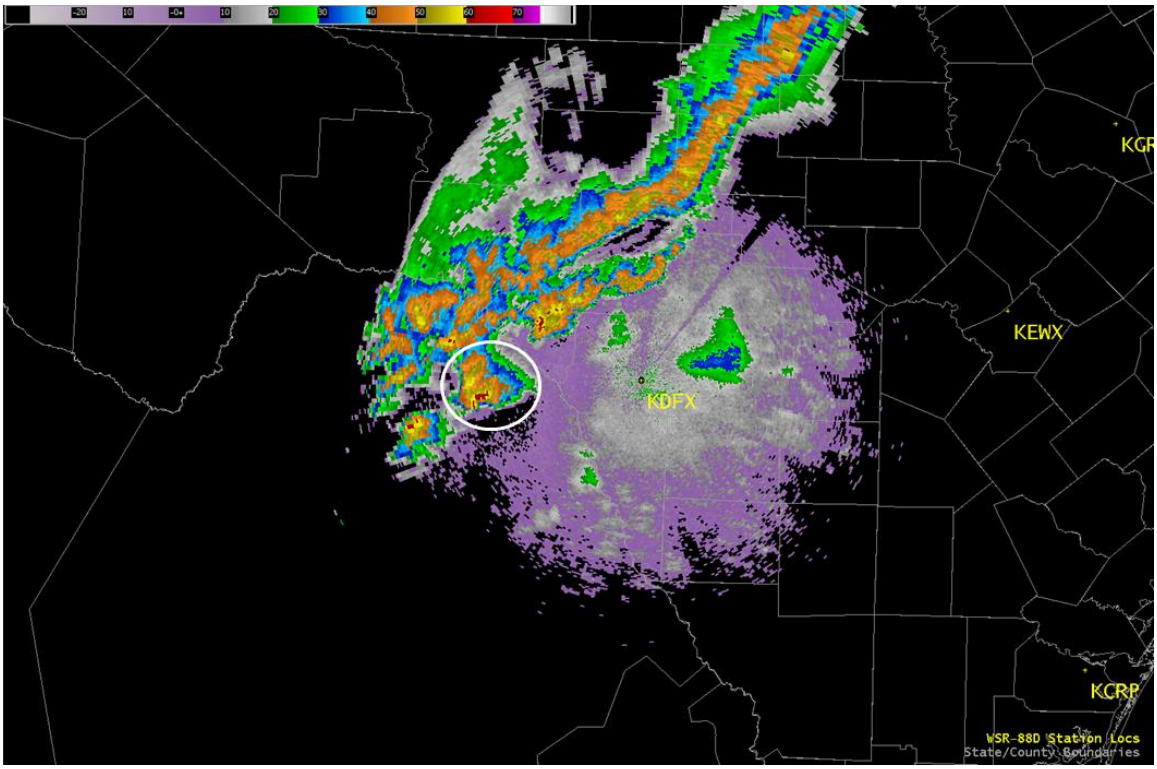

Figure 16: Values of radar reflectivity (dBZ) at a 0.5 degree tilt, from the WSR-88D at Laughlin Air Force Base, TX, for 0200 UTC 18 April 2019. This is a still image of a loop that extends from 2248 UTC 17 April 2019 to 0242 UTC 18 April 2019. A potential supercell is within the white circle. *Click on the image to open animation and enlarge.*

4. Discussion

a. Forecaster perspective

As already mentioned, forecasting, warning, and providing impact decision support service (IDSS; NWS 2018) are a substantial challenge for an area adjacent to, and in many cases, downstream of a data-poor area. In fact, the desert climate of northern Mexico and low population density (except along the Rio Grande) leads to a lack of surface, aircraft, and upper-air observations. While the KDFX (Laughlin Air Force Base, TX) radar and KDRT (Del Rio, TX) upper air station are well placed to observe the atmosphere in the local vicinity, satellite observations are critical to the assessment and forecasting of weather.

Similar to the event on 17–18 April 2019, severe convection and flash flooding are common to this area. Marshall and Eblen (2008) document the EF3 Rosita Valley tornado, while Barrett et al (2017) document the environmental conditions for the F3 Ciudad Acuña tornado and perform modeling to test the sensitivity to terrain and convective initiation. NWS (2013) documents a significant flash and river flood at Eagle Pass, TX, on 14–15 June 2013. Edwards (2006) and Weiss and Zeitler (2008) performed climatological studies of supercells forming over or near the Serranias Del Burro Mountains of northern Coahuila, finding 76 individual supercells between 26 January 1996 and 31 May 2007.

While the supercells are generally isolated, the high CAPE and high precipitable-water environment typical for spring and early summer tends to support high-precipitation supercells, thereby bringing all thunderstorm hazards of frequent lightning, large hail, tornadoes, downburst winds, heavy rain, and flash flooding. Thus, while the overall areal coverage and frequency of severe storms may be low, the conditional probability of significant impact is high, once storms have formed.

Due to the high spatial and temporal resolution of GOES-16 along with low latency, effective IDSS for core partners (e.g., emergency mangers, first responders) can be provided in many areas in anticipation of, and during, high-impact severe convection. For example, a local emergency manager would inform a local NWS office of a future outdoor public event. GOES-16 ABI data, like the SWD, has the potential to show a forecaster the location of a horizontal moisture boundary in relation to the public event. A forecaster subsequently provides IDSS by updating a local emergency manager that the public event is near a region where thunderstorms may form. Once convection commences, information may be passed to local emergency managers as to the location and movement of thunderstorms. Further, ABI data may be used to complement radar data, particularly in regions of complex terrain where radar beam blockage occurs.

b. Data assimilation

As discussed earlier, there were a few key features contained in the morphology of convective preconditioning for which ABI provided improved data, compared to previous GOES imagers. Three features that were captured by ABI are the following: 1) western edge of the moist layer over northern Coahuila as seen in imagery of the split window difference, 2) decreasing values, or cooling, of brightness temperatures in low-level water vapor imagery that was collocated with the western edge of the moist layer, and 3) regions of blowing dust. Both (1) and (2) suggested upward motion of parcels in a region coincident with sloping terrain. High-resolution, convection-allowing models, such as the operational High Resolution Rapid Refresh (HRRR; Benjamin et al. 2016) are a tool within which the assimilation of the three features just discussed may benefit numerical weather prediction.

For the case study herein, HRRR forecasts exhibited a lack of convection over northern Coahuila (not shown). Currently, ABI radiance assimilation with the HRRR has yet to be implemented. Plans are to include the assimilation of clear-sky radiances from the three ABI water vapor bands into the parent domain of the HRRR beginning in 2020 (H. Lin, S. Weygandt, M. Hu, A. Back, C. Alexander, and S. Benjamin, personal communication). Assimilation of ABI data along with a linking of variables through the use of a background error covariance has the potential to benefit future HRRR forecasts of convection.

5. Summary and conclusions

Due to advancements in satellite remote sensing of GOES imagers, ABI was shown to capture processes that were associated with convective preconditioning. In particular, previous GOES imagers and sounders would have provided lower-resolution and difficult-to-interpret imagery, due to larger footprints and longer time periods between images. GOES-16 ABI illuminates the details of preconditioning of a convective environment better than previous generations of GOES.

A well-defined western edge of a moist boundary layer over northern Coahuila readily was evident in imagery of the split window difference. As the afternoon progressed, the western edge of the moist layer was seen moving westward toward upward-sloping terrain of a geographical ridge. Collocated with the western edge of the moist layer was evidence of upward vertical motion, as inferred from a relatively

narrow and quasilinear region of decreasing values of brightness temperatures in low-level water vapor imagery. In time, sufficient ascent, along with erosion of a capping inversion, may allow some updrafts to reach the LFC. Some updrafts may appear narrow (Cohen 2000) due to relatively weak ascent and, subsequently, become more susceptible to entrainment of dry air characteristic of an EML via vertical shear. Consequently, cloud remnants form and are, at times, referred to as orphan anvils.

In time, a broader region of cooling was evident in imagery of low-level water vapor, which was consistent with the approach of an upper level trough. Further, two regions of blowing dust, each moving in different directions, were used to infer a wind-shift boundary. One region of blowing dust moved northeastward toward the westward-moving western edge of the moist layer that was located over northern Coahuila. As demonstrated by the time-of-arrival tool in AWIPS, convective initiation may have been anticipated as the region of blowing dust was extrapolated in time to arrive at the moist boundary layer.

With advances in data assimilation techniques, the assimilation of ABI data may aid in the prediction of rapidly evolving processes leading up to the initiation of thunderstorms. All of the above features speak to the ability of imagery from ABI, as opposed to previous GOES imagers and sounders, to be used to monitor the morphology of convective preconditioning of a local environment.

Both the ABI and the VIIRS instruments represent advancements over past satellite sensors. There is a growing effort in the space industry to produce future satellites that are significantly smaller (mass ~10 kg) than current operational environmental LEO satellites; such satellites are termed “small-sats”. Small-sats are being developed and launched at a fraction of the cost and with less risk compared to current operational LEOs that are larger (mass ~1000 kg), more expensive, and have more risk (Ma et al. 2017). As a result, several small-sats may pass over a fixed location, and outside of the high latitudes, to provide high spatial- and temporal-resolution imagery. Perhaps ABI-like looping capabilities will become possible with future constellations of small-sats.

ACKNOWLEDGMENTS

The authors gratefully acknowledge that this research was primarily funded by the NOAA GOES-R Program Office. The views, opinions, and findings in this report are those of the authors, and should not be construed as an official NOAA and or U.S. Government position, policy or decision.

REFERENCES

Apke, J. M., J. R. Mecikalski, K. Bedka, E. W. McCaul Jr., C. R. Homeyer, and C. P. Jewett, 2018: Relationships between deep convection updraft characteristics and satellite-based super rapid scan mesoscale atmospheric motion vector–derived flow. *Mon. Wea. Rev.*, **146**, 3461–3480.

Atkins, N. T., R. M. Wakimoto, and C. L. Ziegler, 1998: Observations of the finescale structure of a dryline during VORTEX 95. *Mon. Wea. Rev*., **126**, 525–550.

Banacos, P. C., and D. M. Schultz, 2005: The use of moisture flux convergence in forecasting convective initiation: Historical and operational perspectives. *Wea. Forecasting.*, **20**, 351–366.

Barrett, B. S., L. M. Farfán, G. B. Raga, and D. H. Hernández, 2017: The unusual early morning tornado in Ciudad Acuña, Coahuila, Mexico on 25 May 2015. *Mon. Wea. Rev*., **145**, 2049–2069.

Bedka, K., E. M. Murillo, C. R. Homeyer, B. Scarino, and H. Mersiovsky, 2018: The above-anvil cirrus plume: An important severe weather indicator in visible and infrared satellite imagery. *Wea. Forecasting*, **33**, 1159–1181.

Benjamin, S. G., and Coauthors, 2016: A North American hourly assimilation and model forecast cycle: The Rapid Refresh. *Mon. Wea. Rev*., **144**, 1669–1694.

Bikos, D., J. F. Weaver, and J. Braun, 2006: The role of GOES satellite imagery in tracking low-level moisture. *Wea. Forecasting*, **21**, 232–241.

Bluestein, H. B., E. W. McCaul Jr., G. P. Byrd, R. L. Walko, and R. Davies-Jones, 1990: An observational study of splitting convective clouds. *Mon. Wea. Rev.*, **118**, 1359–1370.

Carlson, T. N., and F. H. Ludlam, 1968: Conditions for the occurrence of severe local storms. *Tellus*, **20**, 203–226.

——, S. G. Benjamin, G. S. Forbes, and Y. F. Li, 1983: Elevated mixed layers in the regional severe storm environment: Conceptual model and case studies. *Mon. Wea. Rev.*, **111**, 1453–1473.

Chesters D., L. W. Uccelliini, and W. D. Robinson, 1983: Low-level water vapor fields from the VISSR atmospheric sounder (VAS) "split window" channels. *J. Clim. Appl. Meteor.*, **22**, 725–743.

Childs, P. P., A. L. Qureshi, S. Raman, K. Alapaty, R. Ellis, R. Boyles, and D. Niyogi, 2006: Simulation of convective initiation during IHOP_2002 using the flux-adjusting surface data assimilation system (FASDAS). *Mon. Wea. Rev.*, **134**, 134–148.

Cintineo, J. L., M. J. Pavolonis, J. M. Sieglaff, and D. T. Lindsey, 2014: An empirical model for assessing the severe weather potential of developing convection. *Wea. Forecasting*, **29**, 639–653.

——, and Coauthors, 2018: The NOAA/CIMSS ProbSevere Model: Incorporation of total lightning and validation. *Wea. Forecasting*, **33**, 331–345.

Cohen, C., 2000: A quantitative investigation of entrainment and detrainment in numerically simulated cumulonimbus clouds. *J. Atmos. Sci.*, **57**, 1657–1674.

Edwards, R., 2006: Supercells of the Serranias del Burro (Mexico). Preprints, *23rd Conf. on Severe Local Storms*, St. Louis, MO, Amer. Meteor. Soc., 6.2.

Farrell, R. J., and T. N. Carlson, 1989: Evidence for the role of the lid and underrunning in an outbreak of tornadic thunderstorms. *Mon. Wea. Rev.*, **117**, 857–871.

Gitro, C. M., D. Bikos, E. J. Szoke, M. L. Jurewicz Sr., A. E. Cohen, and M. W. Foster, 2019: New satellite technology and products to help in the identification and tracking of the elevated mixed layer. *J. Oper. Meteor.*, **7** (13), 180–192.

Goodman, S. J., and Coauthors, 2012: The GOES-R Proving Ground: Accelerating user readiness for the next-generation geostationary environmental satellite system. *Bull. Amer. Meteor. Soc.*, **97**, 1029–1040.

Gravelle, C. M., K. J. Runk, K. L. Crandall, and D. W. Snyder, 2016: Forecaster evaluations of high temporal satellite imagery for the GOES-R era at the NWS operations proving ground. *Wea. Forecasting*, **31**, 1157–1177.

Hillger D. W., and T. H. Vonder Haar, 1977: Deriving mesoscale temperature and moisture fields from satellite radiance measurements over the United States. *J. Appl. Meteor.*, **16**, 715–726.

Houston, A. L., and D. Niyogi, 2007: The sensitivity of convective initiation to the lapse rate of the active cloud-bearing layer. *Mon. Wea. Rev.*, **135**, 3013–3032.

Johnson, R. H., and B. E. Mapes, 2001: Mesoscale processes and severe convective weather. *Severe Convective Storms*, *Meteor. Monogr.*, No. 50, Amer. Meteor. Soc., 71–122.

Kalluri, S., and Coauthors, 2018: From photons to pixels: Processing data from the Advanced Baseline Imager. *Remote Sens.*, **10**, 1–28.

Lanicci, J. M., and T. T. Warner, 1991a, A synoptic climatology of the elevated mixed-layer inversion over the southern Great Plains in spring. Part I: Structure, dynamics, and seasonal evolution. *Wea. Forecasting*, **6**, 181–197.

——, and ——, 1991b: A synoptic climatology of the elevated mixed-layer inversion over the southern Great Plains in spring. Part III: Relationship to severe-storms climatology. *Wea. Forecasting*, **6**, 214–226.

Lindsey, D., D. Bikos, and L. Grasso, 2018: Using the GOES-16 split window difference to detect a boundary prior to cloud formation. *Bull. Amer. Meteor. Soc.*, **99**, 1541–1544.

——, L. Grasso, J. F. Dostalek, and J. Kerkmann, 2014: Use of the GOES-R split window difference to diagnose deepening low-level water vapor. *J. Appl. Meteor. Climatol.*, **53**, 2005–2016.

Line, W. E., T. J. Schmit, D. T. Lindsey, and S. J. Goodman, 2016: Use of geostationary super rapid scan satellite imagery by the Storm Prediction Center. *Wea. Forecasting*, **31**, 483–494.

Liou, K., 1980: *An Introduction to Atmospheric Radiation*. Academic Press, 392 pp.

Ma, Y., X. Zou, and F. Weng, 2017: Potential applications of small satellite microwave observations for monitoring and prediction global fast-evolving weathers. *IEEE J. Select Topics*, **10**, 2441–2451, doi: 10.1109/JSTARS.2017.2663335.

Madaus, L. E., and G. J. Hakim, 2016: Observable surface anomalies preceding simulated isolated convective initiation. *Mon. Wea. Rev.*, **144**, 2265–2284.

——, G. J. Hakim, and C. F. Mass, 2014: Utility of dense pressure observations for improving mesoscale analyses and forecasts. *Mon. Wea. Rev.*, **142**, 2398–2413.

Marshall, T. P. and L. Eblen, 2008. The Rosita Valley, TX tornado: 24 April 2007. Preprints, *24th Conf. on Severe Local Storms*, Savannah, GA, Amer. Meteor. Soc., P3.2.

Mass, C. F., and L. E. Madaus, 2014: Surface pressure observations from smartphones: A potential revolution for high-resolution weather prediction? *Bull. Amer. Meteor. Soc.*, **95**, 1343–1349.

McMillin L. M., D. S. Crosby, and M. D. Goldberg, 1995: A water vapor index from satellite measurements. *J. Appl. Meteor.*, **34**, 1551–1558.

Mecikalski, J. R., and K. M. Bedka, 2006: Forecasting convective initiation by monitoring the evolution of moving cumulus in daytime GOES imagery. *Mon. Wea. Rev.*, **134**, 49–78.

——, ——, S. J. Paech, and L. A. Litten, 2008: A statistical examination of GOES cloud-top properties for nowcasting convective initiation. *Mon. Wea. Rev.*, **136**, 4899–4914.

——, J. K. Williams, C. P. Jewett, D. Ahijevych, A. LeRoy, and J. R. Walker, 2015: Probabilistic 0–1-h convective initiation nowcasts that combine geostationary satellite observations and numerical weather prediction model data. *J. Appl. Meteor. Climatol.*, **54**, 1039–1059.

Negri, A. J., and T. H. Vonder Haar, 1980: Moisture convergence using satellite-derived wind fields: A severe local storm case study. *Mon. Wea. Rev.*, **108**, 1170–1182.

NWS, 2013: June 14–15, 2003 flash flood event. NOAA/NWS Austin-San Antonio Weather Forecast Office, New Braunfels, TX, 7 pp. [Available online at https://www.weather.gov/media/ewx/wxevents/ewx-20130615.pdf.]

——, 2018: Service description document (SDD) impact-based decisions support services for NWS core partners. [Available online at http://www.nws.noaa.gov/im/IDSS_SDD_V1_0.pdf.]

Purdom, J. F. W., 1976: Some uses of high-resolution GOES imagery in the mesoscale forecasting of convection and its behavior. *Mon. Wea. Rev.*, **104**, 1474–1483.

Rao, A. P., H. E. Fuelberg, 1997: Diagnosing convective instability from GOES-8 radiances. *J. Appl. Meteor.*, **36**, 350–364.

Ribeiro, B. Z., and L. F. Bosart, 2018: Elevated mixed layers and associated severe thunderstorm environments in South and North America. *Mon. Wea. Rev.*, **146**, 3–28.

Schmit, T. J., P. Griffith, M. W. Gunshor, J. M. Daniels, S. J. Goodman, and W. J. Lebair, 2017: A closer look at the ABI on the GOES-R series. *Bull. Amer. Meteor. Soc.*, **98**, 681–698.

——, S. S. Lindstrom, J. J. Gerth, and M. M. Gunshor, 2018: Applications of the 16 spectral bands on the Advanced Baseline Imager (ABI). *J. Oper. Meteor.*, **6**, 33–46.

Setvák, M., K. Bedka, D. T. Lindsey, A. Sokol, Z. Charvát, J. Šťástka, and P. K.Wang, 2013: A-Train observations of deep convective storm tops. *Atmos. Res.* **123**, 229–248.

Walker, J. R., W. M. MacKenzie Jr, J. R. Mecikalski, and C. P. Jewett, 2012: An enhanced geostationary satellite-based convective initiation algorithm for 0–2 h nowcasting with object tracking. *J. Appl. Meteor. Climatol.*, **51**, 1931–1949.

Weiss, J. and J. Zeitler, 2008: Supercells of the Serranias del Burro. Preprints, *24th Conf. on Severe Local Storms*, Savannah, GA, Amer. Meteor. Soc., 17A.4.

Weldon, R. B., and S. J. Holmes, 1991: Water vapor imagery—Interpretation and applications to weather analysis and forecasting. NOAA Tech Rep. NESDIS 57, 213 pp.

Xue, M. and W. J. Martin, 2006: A high-resolution modeling study of the 24 May 2002 dryline case during IHOP. Part II: Horizontal convective rolls and convective initiation. *Mon. Wea. Rev.*. **134**, 172–191.

Zehr, M. R., J. F. W. Purdom, J. F. Weaver and R. N. Green, 1988: Use of VAS data to diagnose the mesoscale environment of convective storms. *Wea. Forecasting.*, **3**, 33–49.

REVIEWER COMMENTS

[Authors' responses in *blue italics.*]

REVIEWER A (Peter C. Banacos):

Initial Review:

Recommendation: Accept with minor revisions.

Synopsis: This case study uses a satellite perspective (mainly GOES-16) to highlight atmospheric features relevant to the preconditioning and eventual initiation of deep moist convection over northern Coahuila/southern Texas on 17 April 2019. Sharp moisture gradients, a deepening PBL, and inferred strengthening horizontal convergence along the eastern slopes of the Serranias Del Burro Mountains are a central theme. Many features are assessed utilizing the split window difference (SWD) imagery, which represents a difference in brightness temperatures between the 10.3–12.3 μm channels in the infrared range.

In my opinion, this is a useful case study and worthy of publication in EJSSM. The work advocates for the utility of new products available on the modern GOES-R satellite series. From an operational perspective, it is instructive to see application of the GOES Advanced Baseline Imagery (ABI) data for important forecast challenges (e.g., convective initiation). The authors have done a good job; most of my comments involve organizational aspects of the manuscript. Also, the operational discussion (section 4) could benefit from a more direct comparing and contrasting of the ABI vs. radar data in the context of assessing the potential for convective initiation.

Major Comments: The example use of the SWD data is instructive, but [notably] diagnostic conditions associated with this case were nearly optimal. On 17 April 2019, we have a cloud-free air mass, over elevated and sharply sloping terrain, involving a pronounced dryline. While a good example of SWD application, the boundary layer changes (deepening and moistening) are ideally observed in this scenario. The authors briefly touch on this point (Page 14, first paragraph, somewhat randomly using the orography of eastern Virginia as an example), but the strengths and weaknesses of the SWD for this application could be made more clear for the reader to enhance operational understanding. This could be part of section 4.

I decided to place additional text about the use of the SWD earlier in the paper. In fact, in Section 2 entitled, "Data" the SWD is introduced and defined. I placed text after the paragraph that begins, "SWD imagery from the GOES-R series provides forecasters with a low-latency tool…"

I have a couple of issues with this (section 1) discussion. First, nearly all numerical models (and associated model soundings) can be useful in assessing potential changes to the thermal and moisture profiles in data sparse areas. Such assessments aren't limited to cloud-scale models, as implied.

You're correct; I changed the phrase, "numerical cloud models" to "numerical models" by removing the word "cloud".

Second, at present, most operational forecasters do not have access to cloud-scale model output in real-time or on a routine basis. While this might limit the ability to "see" details in potential entrainment processes in incipient updrafts, entrainment can be inferred in a general sense by the evolution of modeled convection in the commonly available convection allowing models (at 3-4-km horizontal resolution) or from dry layers in model soundings.

[The changed wording] is now consistent with your concern. That is, "...numerical models can be used as guidance..."

There is evidence of transverse waves or bands in the low-level water vapor imagery over northern Coahuila. I'm curious if the authors can provide an explanation for these transverse waves. Also, are the

waves located within the steep lapse rates of the EML (which would generally not be favorable for wave motion) or is this an artifact of something else?

We see waves in imagery often, particularly over terrain ridge lines. Further, waves are also present in inversions were vertical shear is present. Lastly, waves are seen associated with cold fronts moving south along the Rocky Mountains. I have chosen to exclude any discussion about the waves you pointed out, as such a discussion would be a diversion from the main topic. My guess is that the waves are a result of southwesterly flow over the complex terrain of Mexico. That is, the terrain is forcing the waves.

Subsection 4a: As written, this subsection of the manuscript lacks focus. A discussion of the operational benefits of the GOES-16 ABI data is fine, as demonstrated in your case study. However, in my view, the second paragraph unnecessarily veers into aspects of climatological frequency of convective storms in the region. I didn't find much benefit or perspective from the examples cited.

I disagree. Information about convective activity for the region of this study may be useful to some.

In the fourth paragraph, I think the authors can state the benefits of GOES-16 in monitoring convective initiation without conflating the challenges associated with supercell storm motion and storm splitting. While we have some useful guiding principles (e.g., the Bunkers method), the deviant motion of individual cells can be quite difficult to predict and is a very short-range forecast problem in its own right.

You have a good point; the paragraph is mostly about supercell motion. Thus, I removed the paragraph.

Lastly, paragraph five should discuss how these high quality GOES-16 data enhance IDSS, perhaps sharing how it compliments radar data (e.g., monitoring in areas of radar beam blocking or beam overshoot).

Good idea; I added [explanatory] text. [Editor Comment: Quoted text blocks are not reproduced herein, for space considerations.]

The authors claim a relationship between convective updraft width (or "narrowness") and the magnitude of larger-scale ascent. While this may be so, the claim is made without citing work on what controls the width of incipient convective updrafts. Please provide a reference, more clearly describe this claim as speculative, or remove.

Cohen (2000) was added as a reference.

[Minor comments omitted…]

Second Review:

Recommendation: Accept with minor revisions.

General Comment: All of my comments from the original round were adequately addressed. My remaining concerns are grammatical/technical in nature.

[Minor comments omitted…]

REVIEWER B (John R. Mecicalski):

Initial Review:

Recommendation: Accept with minor revisions.

Overall: This paper is well written, and overall is appropriate for publication in the "*Electronic Journal of Severe Storms Meteorology*", especially given the focus on the pre-convective severe-storm environment. I

particularly like the focus outside the U.S., where satellite data will always "win" over nonexistent or poor radar-coverage situations. I also am happy to see the focus by on the relatively uncommon use of the water vapor imagery in the NWS. I do appreciate the analysis on changing brightness temperatures as related to deepening EMLs and how brightness temperatures behaving in regions of blowing dust, which are rarely discussed(!). As a result, I only have minor comments, which once addressed, I feel the paper will be ready for publication.

[Minor comments omitted…]

Second Review:

Recommendation: Accept.

General Comment: I am happy with how the authors have addressed my comments, and after re-reading the updated paper, there are no additional changes, so I will accept the paper in its present form.

REVIEWER C (Michael A. Bowlan):

Initial Review:

Recommendation: Accept with minor revisions.

Scientific Comments: Overall, I feel that the scientific content of this paper is solid. Plenty of references are used to set the stage for the case study and to give a good introduction to the improvements of satellite data for use in short-term severe-storm forecasting. I like that this paper goes through a good operational example of a forecast problem that is very common across different regions of the country, and shows how the new satellite data can be used in the absence of and in addition to other observations, when trying to predict CI. I think the results shown here in this paper are very relevant across the weather service and will serve to show other forecasters new ways that this data can be used for the complicated problem of convective initiation.

Pretty much all of my comments are technical, as I think the scientific aspect of this case study is solid, and I agree with the assertions made throughout the paper. More and more case studies across more regions should be examined in the future, to see the differences and similarities in using the SWD to anticipate convective initiation. As is stated in the paper, this is a technique that can prove useful at times when looking for CI, but at other times, many of these signals don't exist in the satellite imagery prior to convective initiation. I know from my time looking at these products in the testbed that the SWD, many times [they don't] show this enhanced signal, even in clear skies along boundaries, prior to CI. I would be interested to see more research, using real examples now from GOES-16/17, into how differing boundary-layer environments play a role into what type of signal can be expected from the SWD.

I enjoyed this case study, and liked how the satellite data was on full display throughout the paper to show the utility of the improvements of the GOES-R series. Since the point of this paper is just to show a case study, I think that it does that very well, while following the science that has already been published on using the SWD and low-level water vapor channel, and what certain features mean in those products.

[Minor comments omitted…]

Second Review:

Recommendation: Accept.

General Comment: I am good with the edits made and the justification provided. I think this paper is good for publication from my end.